Nanometer Axial Resolution by Three-Dimensional Supercritical Angle Fluorescence Microscopy

Christian M. Winterflood, Thomas Ruckstuhl, Dorinel Verdes, and Stefan Seeger*

Physikalisch-Chemisches Institut, Universität Zürich, Winterthurerstrasse 190, CH-8057 Zürich, Switzerland

(Received 26 February 2010; published 31 August 2010)

We report a noninvasive fluorescence microscopy method and demonstrate nanometer resolution along the optical axis. The technique is based on the influence of the microscope slide on the angular intensity distribution of fluorescence. Axial positions are determined by measuring the proportion of light emitted below the critical angle of total internal reflection, which behaves in a classical way, and light emitted above the critical angle, which is exponentially dependent on the distance of the fluorophore from the microscope slide.

DOI: 10.1103/PhysRevLett.105.108103 PACS numbers: 87.64.M−, 68.37.Uv

Fluorescence microscopy is a powerful tool in biology, providing noninvasive imaging with high biomolecular specificity. The diffraction-limited resolution of standard fluorescence microscopy, 200 nm in the lateral and 500 nm in the axial direction, is insufficient to study the organization of the cell at the molecular level. To this end, several super-resolution microscopy techniques have been introduced that circumvent the diffraction-barrier. Stimulated emission depletion (STED) microscopy was the first to achieve super-resolution by far-field optics and has attained 20 nm lateral resolution [1]. 4Pi microscopy has shown 40–45 nm in all three dimensions in combination with STED [2]. More recently, stochastic optical reconstruction microscopy (STORM) [3] and photoactivated localization microscopy (PALM) [4] have achieved lateral resolutions of 20 nm based on single-molecule localization of photoswitchable fluorescent labels. Extensions of the latter techniques have attained an axial resolution of 50 nm using lens astigmatism [5], 75 nm using double-plane detection [6] and sub-20 nm axial resolution using photon self-interference [7] or a double-helix point spread function [8]. In differential evanescence nanometry (DiNa) [9] the exponential decay of the evanescent field created by total internal reflection fluorescence (TIRF) illumination at the surface is used to measure positions with 10 nm accuracy along the optical axis (z axis). The intensity obtained from a fluorescent particle located within the evanescent field is not only subject to its distance from the surface but is also to its intrinsic brightness. Therefore, the intensity of the TIRF image is calibrated with a consecutive fluorescence image obtained with wide-field illumination. The prerequisite of stable fluorescence intensities hampers the use of TIRF for z localization of fluctuating emitters, such as single fluorophores, photoswitchable labels, and quantum dots.

The discontinuity of the refractive index (RI) at the interface between an aqueous sample and glass has a strong impact on the angular distribution of radiation of fluorophores nearby. Fluorophores located within one emission wavelength λ from a glass interface, emit a significant proportion of their fluorescence above the critical angle θ_c into the glass. For fluorophores located directly above the glass, supercritical angle fluorescence (SAF) accounts for 34% of their total emission. The electromagnetic coupling of the dipole emitter's near-field with the glass decays rapidly with its surface distance z and at a distance of one emission wavelength SAF is already below 2% of the total emission [10,11]. Consequently, exclusive collection of SAF leads to a high surface-confinement of the detection volume which is useful for biosensing [12], surface-selective cell imaging [13] and diffusion measurements in membranes [14].

Here we introduce three-dimensional SAF microscopy (3D-SAFM) for z localization with nanoscale resolution. It is based on simultaneous fluorescence collection in separate angular regions, below and above the critical angle for total internal reflection $\theta_c = \sin^{-1}(n_2/n_1)$, where n_1 and n_2 are the RIs of the glass substrate and the sample medium, respectively. The principle of 3D-SAFM is illustrated in Fig. 1. SAF provides an extremely sensitive measure of the z position due to its rapid decay along the z axis. The fluorescence emission into surface angles below θ_c, referred to as undercritical angle fluorescence (UAF) [15], is not influenced by an emitter's z position [16] and can therefore be used to measure its intrinsic brightness [Fig. 1(a)]. The parallel detection of SAF and UAF makes it possible to account for fluorescence intensity fluctuations of small emitters on any time scale. The z position is obtained from the measurement of the SAF/UAF ratio and the theory of its decay along the optical axis.

3D-SAFM was accomplished on a sample-scanning (Märzhäuser, ScanIM) fluorescence microscope with a custom-made objective [17,18] consisting of an aspheric lens (N.A. 0.62 or 24° angular aperture, LightPath Technologies, lens 350340) and a parabolic collector as shown in Fig. 1(b). The aspheric lens focuses a laser beam (635 nm, Picoquant, LDM635) with near-diffraction-limited performance onto the surface of a coverslip. The

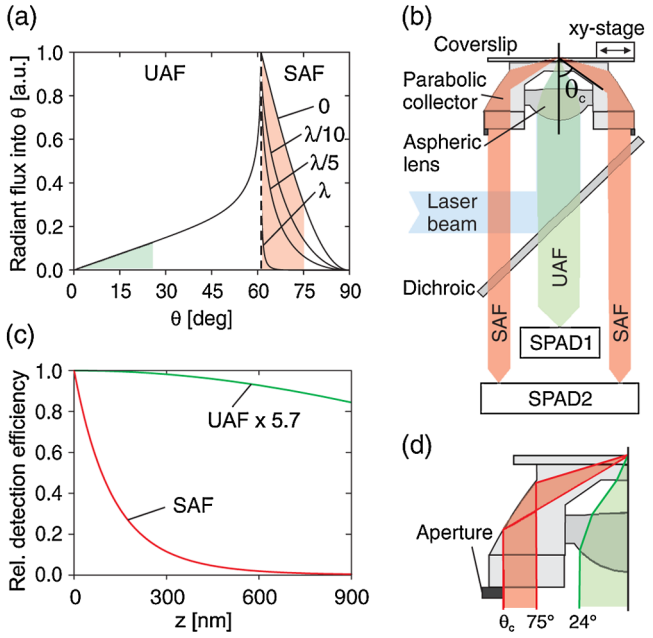

FIG. 1 (color online). Principles of 3D-SAFM. (a) Radiant flux into angles θ from the optical axis of a fluorophore with randomized orientation at different distances z from a water-glass interface ($\theta_c = 61.1°$, dashed line) in fractions of λ. SAF emission is significantly reduced already for small distances, while UAF emission is unaltered. The indicated areas represent the portions captured by the objective. (b) Optical setup. (c) Simulated z dependence of the relative detection efficiencies of SAF and UAF for Cy5 ($\lambda = 670$ nm) for water-glass. The moderate decline of UAF follows the laser intensity distribution near the surface. (d) Enlarged view of the optical paths.

focus has a lateral and axial extent of 433 ± 8 nm and 2.5 μm ($1/e^2$ intensity), respectively. SAF is collected by the parabolic element and UAF by the aspheric lens. Both signals are detected with single-photon avalanche diodes (Perkin Elmer, SPCM-AQR-13) with the small diameter (180 μm) of the photosensitive area acting as a spatial filter. The separate optical paths for near- and far-field emission generate two overlapping fluorescence detection volumes of completely different axial extent. The decays of the relative detection efficiencies for SAF and UAF along the z axis are shown in Fig. 1(c). The z decay of SAF was calculated in a classical electrodynamic framework, where the fluorescing molecule is considered as a radiating electric dipole. The flux intensity of the radiation into angles collected above θ_c was calculated according to Ref. [11] assuming a randomized dipole orientation. The z decay of UAF was computed as the product of the spatial excitation intensity distribution calculated according to Refs. [19–22] and the spatial collection efficiency function calculated according to Ref. [23]. The decay of the SAF/UAF ratio is dependent on the RI of the sample medium above the coverslip and was calculated according to the experiment.

We validated 3D-SAFM by measuring the z profile of a silica sphere of 5 μm diameter (Polysciences) coated with the fluorescent dye $DiIC_{18}(5)$ [DiD, Invitrogen, (650/670)] [Fig. 2]. The silica bead ($n = 1.429$) was immobilized on a glass coverslip ($n = 1.523 \pm 0.002$) and immersed in an index-matched solution of glycerol/water ($n = 1.429 \pm 0.002$) to avoid any optical influence of the bead. The low angle limit for SAF collection was set to $\theta_c = 69.8 \pm 0.3°$ by means of a circular aperture below the parabolic collector as shown in Fig. 1(d). A scan of the microsphere delivers two images with very different intensity distributions. The depth of the UAF detection volume is about equal to the radius of the sphere and captures the full lateral extent of the bead. In the SAF image only the contact region of the particle with the coverslip appears. The z profile was calculated pixelwise from the SAF and UAF intensities and the theory of their z dependencies, which requires only knowledge of easily accessible experimental parameters such as RIs, collected angles and emission wavelength. As shown in Fig. 2(e), the z profile (points) of the bead is undistorted and follows an ideal sphere (fitted diameter: 5.1 μm) with excellent agreement demonstrating the efficacy of 3D-SAFM. The z values deviate (residuals) at most by ~60 nm, possibly reflecting the roughness of the particle.

To further explore the axial resolution of 3D-SAFM, fluorescent beads of 36 nm diameter (Invitrogen, Fluospheres (650/670)) were used [Fig. 3]. Because of their volume far smaller than the volume occupied by the near-field, the mismatch of their RI with the surrounding

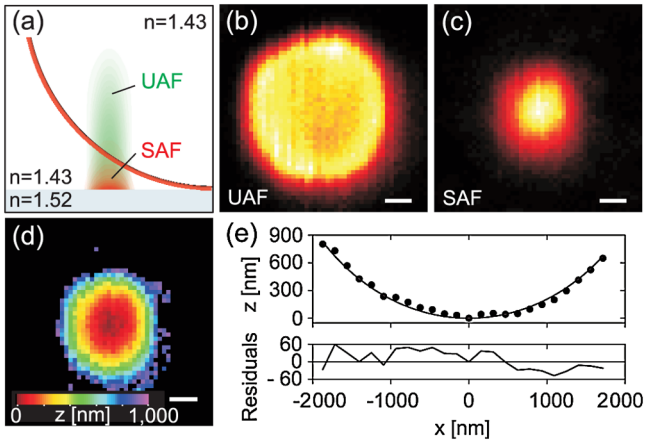

FIG. 2 (color online). 3D-SAFM of a fluorescence coated microsphere of 5 μm diameter. (a) Schematic of the experiment. (b) Raw UAF image. (c) Raw SAF image. (d) 3D image of the bead surface-contact region. Pixels with SAF intensities below a threshold are shown in black. (e) z profile through the center of the bead fitted to a sphere of 5.1 μm diameter. The sample was scanned with a pixel size of 156 nm and 10 ms integration time per pixel. ~1100–2600 counts per pixel were detected in both channels together for determining the z positions. Scale bars = 1 μm.

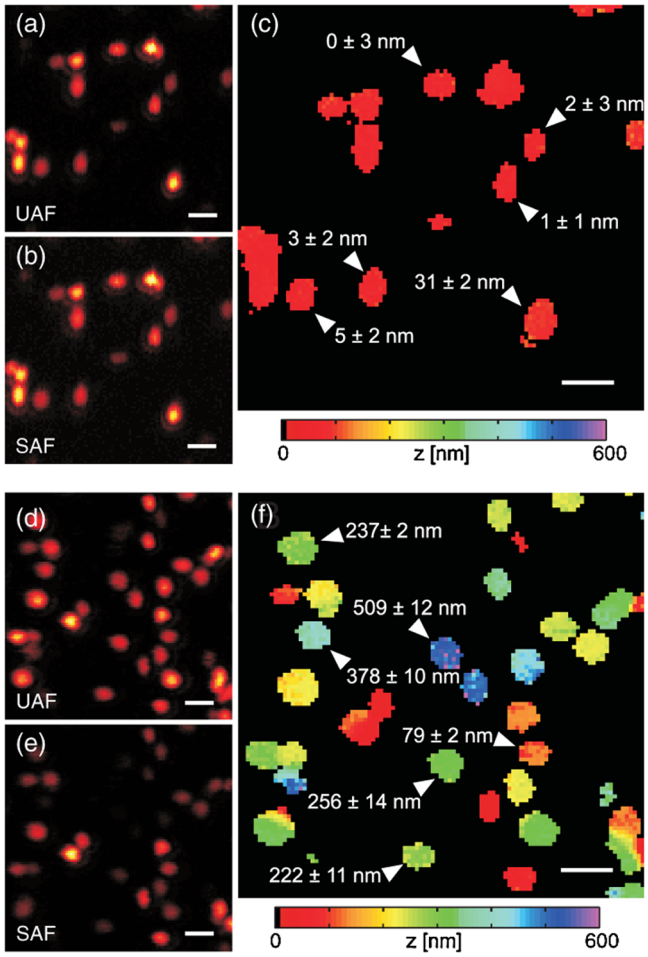

FIG. 3 (color online). 3D-SAFM of 36 nm diameter fluorescent nanospheres. (a) Raw UAF image, (b) Raw SAF image and (c) 3D image of beads adsorbed at the water-coverslip interface. (d) Raw UAF image, (e) Raw SAF image and (f) 3D image of beads embedded in agarose gel. The sample was scanned with a pixel size of 156 nm and 10 ms integration time per pixel. Scale bars = 2 μm.

medium can be neglected. The beads were measured either in water or agarose gel, both having a RI of 1.333 ± 0.002. The low SAF collection angle limit was set to $\theta_c = 61.1 \pm 0.1°$. A narrow z distribution was obtained by nonspecific adsorption of the beads to a water-glass interface. The SAF and UAF images of beads directly at the coverslip surface are indistinguishable when represented with a normalized color map [Figs. 3(a) and 3(b)], but the SAF count rate is approximately 5 times higher because of the higher collection efficiency above θ_c. The 3D image was calculated pixelwise, omitting pixels with a SAF intensity below a threshold [Fig. 3(c)]. The z positions of the indicated beads were calculated from the mean value of their image pixels and the z origin was set to the center of the lowest bead (highest SAF/UAF ratio). Most of the beads were localized within a section of a few nanometers and the variation in the measured z positions is consistent with the size distribution measured with AFM [24]. The indicated errors of 1–3 nm were obtained from the standard error of the mean which represents the localization accuracy of a single scan. It is noteworthy that the accuracy in the z localization is 2 orders of magnitude higher than the diffraction-limited lateral resolution. The localization error was governed by shot noise (~60 000 counts per bead on average) and can be reduced by increasing the number of detected photon counts. The localization error increases with the emitter's surface distance as fewer SAF photon counts are detected. To characterize the localization accuracy deeper inside the sample, a broad z distribution of beads was prepared by embedding them in 1% (w/v) agarose gel ($n = 1.333 \pm 0.001$) [Figs. 3(d)–3(f)]. A film of agarose was prepared by spin coating and then covered with water. As expected, the accuracy decreased along z, but still all beads were localized within an error of 15 nm [Fig. 3(f)].

One can obtain absolute positions with respect to the coverslip surface from the data by precise calibration of both detection efficiencies. However, 3D structures can be resolved accurately even without exact knowledge of ab-

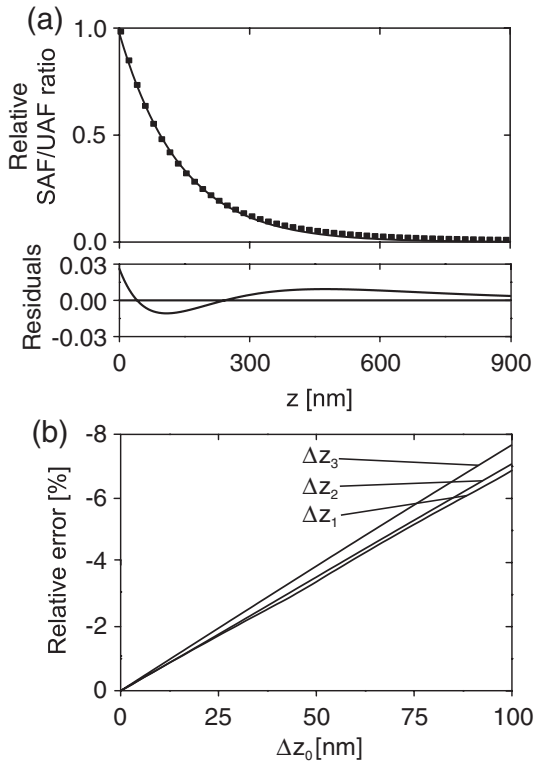

FIG. 4. Axial localization accuracy of 3D-SAFM. (a) The z dependency of the relative SAF/UAF ratio at a water-glass interface for $\lambda = 670$ nm fitted by a monoexponential function (solid line). (b) The relative error of the distance measured between two points separated axially by $\Delta z_1 = 10$ nm, $\Delta z_2 = 50$ nm, and $\Delta z_3 = 200$ nm as a function of the error Δz_0 in establishing the z origin. Even for a very large Δz_0 of 100 nm the relative error of the distance measured between two points is below 8%.

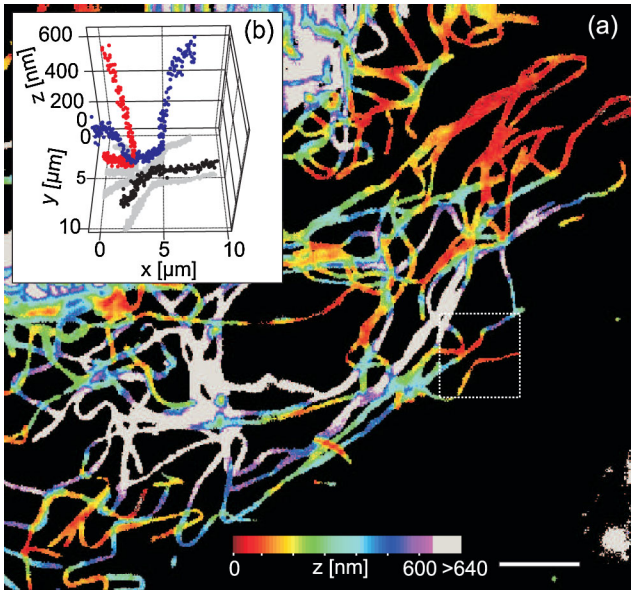

FIG. 5 (color online). 3D-SAFM of the microtubule network of a mouse embryonic fibroblast cell. Microtubules further away than 640 nm from the coverslip surface (corresponding to $<2\%$ of the normalized SAF/UAF ratio) are shown in gray. (Inset) 3D representation of the pixels in the region outlined by the box. The sample was scanned with a pixel size of 156 nm and 3 ms integration time per pixel. Scale bar $= 10\ \mu$m.

solute emitter-coverslip distances due to the quasi monoexponential z decay of the SAF/UAF ratio [Fig. 4(a)]. The proportionality of the SAF/UAF ratios of two axially separated point sources is in good approximation constant, irrespective of their distance from the surface [Fig. 4(b)]. In most cases the highest measured SAF/UAF ratio, e.g., from a contact point of the fluorescent sample with the coverslip, can be used directly to establish the z origin.

Figure 5 shows 3D-SAFM of the microtubule network of an embryonic NIH 3T3 fibroblast cell by indirect immunofluorescence using a Cy5 labeled (650/670) secondary antibody. In immunostaining the cell membrane is permeabilized allowing for antibodies to enter. As a consequence the interior of the cell is RI matched with the aqueous buffer. The antibody-stained microtubules have a diameter of $\sim$60 nm. The bulk of the network is located within the first wavelength from the coverslip and can be z localized. Some microtubules further afar cannot, yet they are imaged by UAF. At the crossings of axially overlapping microtubules the calculated z position represents an average value. The use of photoswitchable dyes can provide a way to resolve such axially overlapping objects. By rapid consecutive single-molecule localization of a large number of fluorophores an image can be reconstructed as done in STORM and PALM. For this purpose a SAF microscope objective with high N.A. optics for UAF is in development. Furthermore, we note that 3D-SAFM is not restricted to the use of parabolic collectors and could be performed with conventional microscope objectives of sufficiently large (N.A. > 1.45). The presented concept of simultaneous detection of SAF and UAF is very generic and can be combined with established super-resolution microscopy techniques including STED.

In conclusion, with 3D-SAF microscopy we have introduced a simple method for noninvasive surface-selective 3D imaging with nanometer axial resolution.

This work was supported by the Swiss National Science Foundation. The authors thank T. Strassen for providing the cell strains and assistance with cell culturing.

*s.seeger@pci.uzh.ch

[1] G. Donnert, J. Keller, C. A. Wurm, S. O. Rizzoli, V. Westphal, A. Schönle, R. Jahn, S. Jakobs, C. Eggeling, and S. W. Hell, Biophys. J. **92**, L67 (2007).
[2] R. Schmidt, C. A. Wurm, S. Jakobs, J. Engelhardt, A. Egner, and S. W. Hell, Nat. Methods **5**, 539 (2008).
[3] M. J. Rust, M. Bates, and X. Zhuang, Nat. Methods **3**, 793 (2006).
[4] E. Betzig, G. H. Patterson, R. Sougrat, O. W. Lindwasser, S. Olenych, J. S. Bonifacino, M. W. Davidson, J. Lippincott-Schwartz, and H. F. Hess, Science **313**, 1642 (2006).
[5] B. Huang, W. Wang, M. Bates, and X. Zhuang, Science **319**, 810 (2008).
[6] M. F. Juette, T. J. Gould, M. D. Lessard, M. J. Mlodzianoski, B. S. Nagpure, B. T. Bennett, S. T. Hess, and J. Bewersdorf, Nat. Methods **5**, 527 (2008).
[7] G. Shtengel *et al.*, Proc. Natl. Acad. Sci. U.S.A. **106**, 3125 (2009).
[8] S. R. P. Pavani, M. A. Thompson, J. S. Biteen, S. J. Lord, N. Liu, R. J. Twieg, R. Piestun, and W. E. Moerner, Proc. Natl. Acad. Sci. U.S.A. **106**, 2995 (2009).
[9] S. Saffarian and T. Kirchhausen, Biophys. J. **94**, 2333 (2008).
[10] W. Lukosz and R. E. Kunz, J. Opt. Soc. Am. A **67**, 1607 (1977).
[11] J. Enderlein, T. Ruckstuhl, and S. Seeger, Appl. Opt. **38**, 724 (1999).
[12] T. Ruckstuhl, J. Enderlein, S. Jung, and S. Seeger, Anal. Chem. **72**, 2117 (2000).
[13] D. Axelrod, J Biomed. Opt. **6**, 6 (2001).
[14] J. Ries, T. Ruckstuhl, D. Verdes, and P. Schwille, Biophys. J. **94**, 221 (2008).
[15] T. P. Burghardt and K. Ajtai, J Biomed. Opt. **14**, 034036 (2009).
[16] L. Novotny, J. Opt. Soc. Am. A **14**, 91 (1997).
[17] T. Ruckstuhl and D. Verdes, Opt. Express **12**, 4246 (2004).
[18] D. Verdes, T. Ruckstuhl, and S. Seeger, J Biomed. Opt. **12**, 034012 (2007).
[19] B. Richards and E. Wolf, Proc. R. Soc. A **253**, 358 (1959).
[20] P. Török, P. Varga, Z. Laczik, and G. R. Booker, J. Opt. Soc. Am. A **12**, 325 (1995).
[21] H. Ling and S.-W. Lee, J. Opt. Soc. Am. A **1**, 965 (1984).
[22] L. Novotny, *Lecture Notes on Nano-optics* (Rochester University, New York, 2000).
[23] J. Enderlein, Opt. Lett. **25**, 634 (2000).
[24] S. Seiffert and W. Oppermann, Polymer **49**, 4115 (2008).